Complement receptor 3 forms a compact high affinity complex with iC3b

Rasmus K. Jensen[1], Goran Bajic[2,3], Mehmet Sen[4], Timothy A. Springer[5,6], Thomas Vorup-Jensen[7], Gregers R. Andersen[1]*

[1] Department of Molecular Biology and Genetics, Aarhus University, Denmark

[2] Laboratory of Molecular Medicine, Boston Children's Hospital, Harvard Medical School, Boston, MA 02115, USA

[3] Department of Pediatrics, Harvard Medical School, Boston, MA, 02115, USA

[4] Department of Biology and Biochemistry, University of Houston, Houston, TX, 77204, USA

[5] Department of Biological Chemistry and Molecular Pharmacology, Harvard Medical School, Boston, MA 02115, USA

[6] Program in Cellular and Molecular Medicine, Boston Children's Hospital, Boston, MA, USA

[7] Department of Biomedicine, Aarhus University, Denmark

* Corresponding author. Email: gra@mbg.au.dk

Running title: Characterization of the CR3:iC3b complex

Keywords: Innate Immunity, Complement, Integrin, Structural biology, Surface Plasmon Resonance

Abstract

Complement receptor 3 (CR3, also known as Mac-1, integrin $\alpha_M\beta_2$, or CD11b/CD18) is expressed on a subset of myeloid and certain activated lymphoid cells. CR3 is essential for the phagocytosis of complement-opsonized particles such as pathogens and apoptotic or necrotic cells. The receptor recognizes cells opsonized with the complement fragment iC3b and to a lesser extend C3dg. While the interaction between the iC3b thioester domain and the ligand binding CR3 α_M I-domain is now structurally well characterized, additional CR3-iC3b interactions lack structural insight. Using an integrated structural biology approach, we analyze the interaction between iC3b and the headpiece fragment of the CR3 ectodomain. Surface plasmon resonance experiments found an affinity of 30 nM of CR3 for iC3b compared to 515 nM for the iC3b thioester domain. The $iC3b_1$ intermediate formed during factor I degradation is shown to be a CR3 headpiece ligand in addition to iC3b and C3dg. Small angle x-ray scattering analysis reveals that in solution the iC3b-CR3 complex is more compact than either of the individual proteins and prior models of the complex derived by electron microscopy. Overall, the data suggest that the iC3b-CR3 complex is structurally ordered and governed by high affinity. The identification of significant CR3-iC3b interactions outside the iC3b TE domain appears as a promising target for future therapeutics interfering specifically with the formation of the CR3-iC3b complex.

Introduction

The complement system is a central part of vertebrate innate immunity. It connects to other branches of the immune system, including adaptive immunity through its functions especially in stimulation of antibody formation. Complement is a tightly regulated proteolytic cascade, which upon activation leads to cleavage of the 186 kDa complement component 3 (C3) into an anaphylatoxin C3a and an opsonin C3b. The C3b fragment is deposited on the surface of the complement activator through covalent bond formation when an activator nucleophile reacts with an exposed thioester (TE) present in the TE domain of nascent C3b. Host cells present glycans that attract fluid phase regular factor H (FH), and also express complement regulators membrane cofactor protein (MCP/CD55) and CR1/CD35. These regulators bind specifically to C3b and enable its degradation by the serine protease factor I (FI). As a result, C3b is quickly converted to iC3b *in vivo* (1), and acts as a powerful opsonin, as it is recognized by CR2 and the two integrin receptors CR3 (also known as Mac-1, CD11b/CD18 or integrin $\alpha_M\beta_2$) and CR4 (p150,95, CD11c/CD18 or integrin $\alpha_X\beta_2$). Whereas C3b has a well-defined conformation, the FI degradation of the C3b through double cleavage within the CUB domain leads to a flexible attachment of the thioester domain to the C3c moiety (2,3).

Recognition of iC3b by CR3 leads to several physiological responses dependent on the cell type and activation state of the CR3-expressing cell, including phagocytosis of dying host cells or pathogens (4,5). CR3 consists of the non-covalently associated α_M and β_2 subunits highly expressed on the plasma membrane of myeloid cells including macrophages, monocytes, dendritic cells and neutrophil granulocytes. Certain lymphoid leukocytes also express CR3 such as natural killer cells and activated T cells, and expression is further inducible in other leukocytes (4,5). CR3 is also highly expressed in microglia, the phagocytes of the central nervous system (CNS), where CR3 mediated phagocytosis of iC3b opsonized presynaptic termini of neurons was recently shown to be important for neural development and homeostasis (6-9). *In vivo* studies leave no doubt about the importance of CR3 supported mechanisms, both as a protective agent against infection (10) or as an aggravating factor in diseases with a poorly regulated inflammatory response, for instance, as observed in animal models of multiple sclerosis and Alzheimer's disease (10,11).

CR3, similar to other integrins, adopts at least three distinct conformations in the cell membrane which controls the activity of the protein. The conformations are known as the bent-closed conformation with low affinity for ligands, the extended-closed conformation which has an

intermediary affinity, and the extended-open conformation with high affinity (Fig. 1A). The conformation of the integrin is controlled through both inside-out signaling, where stimuli received by the cell through other receptors are signaled to the integrin, and outside-in signaling, where a ligand is recognized by the integrin, and the signal is relayed into the cell through changes in integrin conformation (12,13).

An outstanding question is how the CR3 receptor is able to bind many structurally unrelated ligands with more than 50 proteins, carbohydrates and lipidic molecules reported so far (14). In the CR3 α_M chain, the I-domain (α_MI) contains the primary ligand metal ion-dependent binding site (MIDAS) for a plethora of ligands including iC3b, ICAM-1, RAGE, platelet factor 4, mindin, platelet glycoprotein Ib, sialylated FcγRIIA, CD40L, LL-37, LRP1, fibrinogen, and the LukAB cytotoxin (15-24). Upon recognition of ligands inducing outside-in signaling, conformational changes of the loops surrounding the MIDAS in the α_MI leads to a rearrangement of the C-terminal α7-helix, which is shifted 7 Å downwards (25,26). In the $\alpha_{IIB}b_3$ integrin, this allows the MIDAS of the β_2I-like domain to recognize a glutamate in the α_MI α7-helix and induces the open conformation of the β_2 I-like domain that amplifies into a 60° swing-out of the hybrid domain (27). The conformational change is propagated through the legs of the integrin which are separated from each other. This in turn leads to separation of the two cytosolic tails of the integrin and changes in intracellular signaling. In addition to the MIDAS, the β_2 I-like domain has two metal ion binding sites. One which is adjacent to the MIDAS (ADMIDAS) has a negative regulatory role on ligand binding while the ligand-associated metal-ion binding site (LIMBS) has a positive regulatory role. The ADMIDAS site is normally occupied by a Ca^{2+}-ion and removing the ion or replacing it with Mn^{2+} leads to increased affinity towards ligands (28).

We have previously established that the major binding site for the CR3 α_MI is located in the TE domain of iC3b and that this interaction is characterized by a dissociation constant (K_D) of 600 nM (29). Other functional studies (30-33) suggests the existence of one or more additional recognition sites between iC3b and CR3. A recent structural analysis by negative stain electron microscopy (nsEM) of the iC3b-CR3 headpiece complex suggested direct contacts between regions in iC3b close to the C345c domain and the β-propeller/β I-like domain portion of the CR3 headpiece, but a three dimensional reconstruction was not obtained and the presented 2D classes suggested multiple possible orientations of the C3c moiety of iC3b relative to the CR3 headpiece (2).

To investigate whether the iC3b-CR3 complex is an ordered complex with a specific conformation or a flexible ensemble of conformations due to iC3b flexibility, we analyzed the complex between iC3b and the CR3 headpiece in solution through multiple biochemical and biophysical techniques. We now show that the CR3-iC3b interaction is characterized by a 17-fold higher affinity compared to the minimal complex between the iC3b TE domain and the CR3 αM I-domain (29). Small angle x-ray scattering (SAXS) suggests at least one additional protein-protein interface outside the α_MI-TE. We also establish that complete degradation of C3b to iC3b is not required for CR3 interaction since the intermediate $iC3b_1$ is shown to be a CR3 ligand.

Results

Purification and structural characterization of the CR3 headpiece

Stable HEK293S GnTI$^-$ cell line expressing the CR3 headpiece fragment was generated by co-transfection of plasmids encoding the α_M- and β_2-chains of the 140 kDa CR3 headpiece fragment (Fig. 1A). Initially the cells were selected by antibiotic resistance, and subsequently the highest expressing clones were enriched through flow cytometry based on GFP fluorescence. The final selection was performed using sandwich ELISA on the cell supernatant detecting the presence of both the α_M- and β_2-chain. To perform large-scale protein production, the stably transfected cells were adapted to serum-free medium and transferred to suspension. Protein expression yields ranged from 0.75 to 1.25 mg of CR3 headpiece per litre of cell

culture that could be purified in a 3-step purification scheme (Supplementary Fig. 1A). The final size exclusion chromatography (SEC) demonstrated that the resulting CR3 headpiece was monodisperse in a buffer containing 20 mM HEPES pH 7.5, 150 mM NaCl, 5 mM $MgCl_2$, 1 mM $CaCl_2$, and therefore amenable to structural and functional analysis (Supplementary Fig. 1B). The oligomerization state of the CR3 headpiece was further analyzed by analytical SEC in Mn^{2+}, Mg^{2+}, and Ni^{2+}-containing buffers (Fig. 1B). These experiments suggest that at low concentration the CR3 headpiece in both Mg^{2+} and Ni^{2+} mainly eluted as a monomer, but a small dimer fraction was also present. Conversely, in Mn^{2+} CR3 exists mainly as a dimer, with only a small fraction eluting as a monomer. This is in line with prior observations (2), and suggests that the MIDAS and ADMIDAS sites may be important for the dimerization of the CR3 headpiece.

To investigate the structural state of the CR3 headpiece in solution further, synchrotron SAXS analysis was performed. Data were collected on the CR3 headpiece in Mg^{2+} containing buffer within a protein concentration range of 0.7-2.9 mg/mL. Even though the Guinier analysis did not suggest interparticle effects (Fig. 2A), the forward scattering of the CR3 headpiece almost doubled when raising the concentration from 1.1 to 1.7 mg/mL (Fig. 2B). The same trend is observed for both radius of gyration (R_g) and estimated maximum particle diameter (D_{max}). R_g and D_{max} increased from ~68 Å to ~90 Å and 200 Å to 350 Å respectively (Fig. 2C). This is clear evidence of a change in the oligomerization state of CR3, likely to be a transition from a monomeric to a dimeric state. Since at 0.7 mg/mL the I_0 was already 57 % of the I_0 at 2.9 mg/mL, a small fraction of dimer is likely to be present even at low concentration as also observed in the SEC assay (Fig. 1B). The Guinier-normalized Kratky plot indicates that the CR3 headpiece is an ordered protein, but with some flexibility (Fig. 2D). We further investigated the homogeneity of the CR3 headpiece fragment using single-particle negative stain electron microscopy (EM). A majority of the molecules were monomers on the EM grid (Supplementary Fig. 1C), and single particle 2D class averages confirmed that monomers were the dominating state (Fig. 2E) whereas a minor fraction formed dimers (Fig. 2F). In accordance with an earlier study (2), the 2D class averages containing dimers suggested a head-to-tail organization in which the α_MI domain of one CR3 headpiece is interacting with the distal end of the β-leg encompassing the I-EGF1 or PSI domains of the second CR3 headpiece. In our 2D class averages of the CR3 headpiece monomer, both the classical 'open' and 'closed' conformations were observed. This was further verified by 3D classification, where the data set separated clearly into an open conformation expected to have high ligand affinity and a closed conformation likely to have low ligand affinity, with approximately 50% of the particles contributing to each reconstruction (Fig. 2G-H). The size of the 3D envelope is slightly smaller than the D_{max} observed in SAXS (Fig. 2I), which further supports that a small amount of CR3 dimer is present even in the SAXS data recorded at low concentration. Altogether, these data demonstrated that our recombinant CR3 headpiece fragment exists in an equilibrium between the open and the closed conformation, and that the fragment dimerizes in a concentration dependent manner. The equilibrium between the monomer and dimer is sensitive to the nature of the different cations occupying the MIDAS and the ADMIDAS.

The CR3 headpiece forms a stable complex with iC3b and binds with low nanomolar K_D

To verify that the CR3 headpiece is able to form a stable complex with iC3b, we formed the complex and assessed stability on a 2.4 ml SEC column. In a Mg^{2+}-containing buffer, the CR3:iC3b complex elutes in a monodisperse peak containing both proteins at an elution volume 0.1-0.15 ml earlier than either of the two individual proteins (Fig. 3A-B). The SEC profile obtained in a Mn^{2+}-containing buffer (Fig. 3C) was almost identical, showing that iC3b can out-compete the CR3:CR3 dimer even at low concentrations of the complex. We next used surface plasmon resonance (SPR) to measure the affinity and the kinetics of the CR3 headpiece-iC3b interaction. We coupled C3b to biotin through its free thioester cysteine side chain and subsequently converted C3b to iC3b by FI cleavage in the

presence of FH as previously described (34). The biotinylated iC3b was then bound to a streptavidin-coated SPR chip surface. The CR3 headpiece bound iC3b in a Mg^{2+} containing buffer with a dissociation constant $K_D = 30$ nM when fitted to a 1:1 interaction model (Fig. 3D and Table 1). The CR3 headpiece bound to iC3b in a Mn^{2+} containing buffer with a significantly lower k_{on}, presumably due to an increasing content of CR3 headpiece dimers competing with iC3b interaction. In agreement with a competing binding reaction involving formation of CR3 dimers, these data were more difficult to fit with a 1:1 interaction model at higher concentrations of CR3 (Fig. 3E). Taken together with the estimated k_{off} which was also significantly lower than in Mg^{2+}, the CR3 affinity for iC3b in the presence of Mn^{2+} was approximately 5-fold higher with an apparent dissociation constant K_D at 6.2 nM (Fig. 3E and Table 1).

The CR3 headpiece binds stronger to iC3b than to C3d

Because the affinity of the CR3 headpiece binding to iC3b was ~18 fold higher than what we previously described for the isolated CR3 α_MI domain (29), we wanted to investigate whether this was due to stronger binding through the α_MI domain in the context of the CR3 headpiece or whether CR3 contains an additional interaction site for iC3b outside of the α_MI domain. For this purpose, we used the recombinant C3d fragment corresponding to C3dg with the flexible remnants of the C3g fragment removed (29). As above the apparent affinity of the CR3-C3d complex was measured using SPR (Fig. 4A-B). Because the binding kinetics were very fast and data could not be robustly fitted to a 1:1 interaction model, we performed a steady-state analysis and measured an apparent $K_D = 515$ nM similar to the affinity of α_MI domain and iC3b (29). This suggests that embedding of the α_MI into the CR3 headpiece does not significantly change its affinity for the C3d moiety in iC3b. Next, we used an SPR-based competition assay where we measured the binding of the CR3 headpiece to immobilized iC3b in the presence of increasing amounts of free C3b, iC3b and C3d (Fig. 4C-E). Fluid phase iC3b and C3d competed for binding to the immobilized iC3b whereas C3b did not, indicating that the competition was ligand-specific. Soluble-phase iC3b robustly competed for CR3 binding whereas, by contrast, addition of C3d only produced a marginal decrease in the binding signal even at a 50-fold molar excess of C3d. In summary, our SPR data demonstrated that additional contacts, outside of the α_MI domain:TE interface we described by X-ray crystallography (29), contribute to the CR3 interaction with iC3b.

$iC3b_1$ acts as a CR3 ligand and adopts a conformation distinct from both iC3b and C3b

When iC3b is formed from C3b it is first cleaved by FI between Arg1281 (mature numbering) and Ser1282 to generate $iC3b_1$, followed by a second cleavage between Arg1298 and Ser1299 (Supplementary Fig. 2A). The double cleaved iC3b is by far the most abundant product when FH, CR1 and MCP act as cofactors. However, when vaccinia virus complement control protein (VCP) acts as cofactor, the $iC3b_1$ intermediate cleaved only at the first site accumulates (35). The $iC3b_1$ is unable to bind factor B and form AP proconvertase although it was suggested to adopt a C3b-like conformation (3,35). It can be predicted that if $iC3b_1$ indeed contains a folded CUB domain positioned as in C3b, $iC3b_1$ will not be able to interact with CR3 since the α_M I-domain interaction with the $iC3b_1$ TE domain would be sterically unfavorable (29). To investigate this hypothesis, we generated $iC3b_1$ and assessed complex formation by SEC (Fig. 5A-B). The complex elutes significantly earlier than $iC3b_1$ alone and the presence of both CR3 headpiece and $iC3b_1$ in peak fractions was verified by SDS-PAGE analysis (Fig. 5C). To confirm the CR3 interaction, we formed $iC3b_1$ from biotinylated C3b and immobilized it on a streptavidin-coated SPR sensor. Binding analysis revealed that CR3 interacts strongly with $iC3b_1$ in the presence of Mg^{2+} with K_D= 50 nM (Fig. 5D & Table 1). In summary, these data demonstrate that $iC3b_1$ can act as a ligand for CR3 in vitro.

To investigate the structural properties of $iC3b_1$ we crystallized the protein in complex with the C3

specific nanobody hC3Nb1 (34). The diffraction data extended to a maximum resolution of 6 Å (Supplementary Table 1) and the structure was determined by molecular replacement. Due to the limited resolution we only performed rigid body, TLS and grouped B-factor refinement, which led to an R_{free} value of 26.4 %. In agreement with prior findings (3) the crystallized conformation of iC3b1 is very similar to C3b. Superposition of $iC3b_1$ to C3b in complex with hC3Nb1 revealed only slight differences, primarily in the locations of the C345c, CUB and TE domains which could stem from crystal packing effects (Supplementary Fig. 2B-C). The omit density of the CUB domain is excellent considering the resolution and demonstrates that the two β-sheets in the CUB domain are intact (Supplementary Fig. 2D). Importantly, the CUB domain was positioned correctly since omit density corresponding to the N-linked glycosylation was present around Asn917 (Supplementary Fig. 2E). The peptide bond between Arg1281 and Ser1282 was also efficiently cleaved in the crystallized $iC3b_1$ as evidenced by the lack of electron density at the position of Arg1281-Ser1282 taken in the C3b structure of the CUB domain (Supplementary Fig 2F).

Then, to investigate if the unexpected CR3 binding was due to a structural difference between $iC3b_1$ and C3b in solution, we recorded SAXS data on C3b, $iC3b_1$ and iC3b. Guinier analysis did not suggest interparticle effects and C3b, $iC3b_1$ and iC3b exhibited R_g values of 49 Å, 51 Å and 53 Å, respectively (Supplementary Fig. 3A-C). The R_g values for C3b and iC3b are well in line with earlier reports, whereas for $iC3b_1$ the R_g is slightly higher than previously reported (3). Comparison of the scattering curves (Supplementary Fig. 3D) and the Kratky plots (Supplementary Fig. 3E) clearly showed that $iC3b_1$ in solution adopts a structure that is distinct from both C3b and iC3b and the flexibility of $iC3b_1$ is in between that of C3b and iC3b. The difference in flexibility and conformation of $iC3b_1$ as compared to C3b could underlay the ability of $iC3b_1$ to interact with CR3, whereas the C3b-like conformation observed in our crystal structure of iC3b may be stabilized by crystal packing while not being a frequent conformation in solution. Collectively, our data support a model stating that upon cleavage at Arg1281 leading to $iC3b_1$ formation, the C3f containing region of the CUB domain is able to dislocate from the two β-sheets and thereby increase the flexibility of the CUB domain enabling binding of CR3 to the iC3b TE domain (Fig. 5E). Such a model was earlier proposed to explain how Arg1298 in $iC3b_1$ can be accommodated in the active site of factor I (3). Upon the second cleavage at Arg 1298, C3f is released and the CUB domain collapses leading to the complete dislocation of the iC3b TE domain from the MG1 domain directly observed by us and other with electron microscopy and SAXS (2,3).

CR3-bound iC3b is less flexible

To characterize the solution structure of the iC3b:CR3 headpiece complex we performed synchrotron inline SEC-SAXS. The forward scattering elution profile displayed two peaks - the first one corresponding to the complex, and the second one corresponding to excess iC3b (Fig. 6A). The R_g was stable throughout the first peak showing that the complex is not dissociating during the SEC run, consistent with the 30 nM K_D observed by SPR. A Guinier analysis of the scattering curve did not indicate interparticle effects and suggested an R_g of 67 Å for the CR3-iC3b complex (Fig 6B). A comparison of the Guinier normalized Kratky plots for the CR3:iC3b complex and CR3 or iC3b (Figures 6C & Supplementary Fig 4A-B) suggests that the receptor-ligand complex is a significantly less flexible particle than the receptor or iC3b alone. Based on calculation of the pair distribution function the D_{max} of the complex was estimated to 225 Å (Fig. 6D). In support of a well-defined and structurally ordered CR3:iC3b complex, this is only slightly larger than the ~200 Å we observe for both iC3b and the CR3 headpiece monomers (Supplementary Fig. 4C-D). For comparison we also performed SEC-SAXS analysis of the C3d:CR3 complex that compared to the iC3b:CR3 complex lacks the C3c moiety and the degraded CUB domain. Although the forward scattering profile of this complex was more heterogeneous than that of the iC3b:CR3 complex (Supplementary Fig 4E), the region containing the scattering from

the C3d:CR3 complex could be identified through R_g analysis and comparison with the SEC profile for unbound CR3 headpiece (Fig. 1B). Strikingly, the R_g and the D_{max} values of the CR3:iC3b and CR3:C3d complexes (Supplementary Fig 4F-G) are very similar even though the CR3:C3d complex is 150 kDa smaller. This further supports the idea that iC3b and the CR3 headpiece form a compact complex. A comparison of the Guiner normalized Kratky plots for the two complexes also suggests that the CR3:C3d complex is more flexible than the CR3:iC3b complex (Supplementary Fig 4H).

Prior EM data regarding the CR3:iC3b complex were recorded on charged grid surfaces under negative stain conditions. To investigate the shape of the CR3:iC3b in solution conditions close to *in vivo* conditions, we performed *ab initio* modelling, using the DAMMIF program to generate 15 models. The models were subsequently clustered using DAMCLUST, which gave 6 cluster in total, with only one cluster containing more than a single model. The 10 models in this major cluster were averaged and filtered, which resulted in a flat and extended ab initio envelope (Fig. 5E). Due to the low resolution of the *ab initio* model and the well-known flexibility of iC3b, it is not possible to dock atomic models in a unique manner, although the shape of the *ab initio* model indicates that the long axis of the C3c moiety of iC3b is roughly parallel to the longest axis of the CR3 headpiece (Fig 5E). Taken together, our SAXS data support a model in which iC3b harbors additional CR3 interaction sites not present on C3d, and furthermore show that the CR3:iC3b complex is compact, elongated and fairly rigid.

Discussion

Our prior crystal structure of the α_MI -C3d complex and biophysical experiments defined the core of the iC3b-CR3 interaction centered on the coordination of the divalent cation in the α_MI MIDAS by an aspartate from the iC3b TE domain. From a receptor perspective, the biological significance of the iC3b TE-α_MI interface observed by crystallography was in agreement with multiple independent observations. First, deletion of the α_M I-domain significantly weakened the interaction between cells presenting CR3 and immobilized iC3b (31). Second, mutations in the α_MI MIDAS site interfere with binding of iC3b-coated erythrocytes to CR3 expressing cells (36). Third, CR3 binding to multiple ligands may be blocked by antibodies with epitope in the α_M I-domain (15), and finally the ability of the isolated α_M I-domain to bind iC3b in vitro (29). On the iC3b side, we and others demonstrated *in vitro* how C3d and C3dg bound α_M I-domain with an affinity resembling that of the iC3b-α_M I-domain interaction (29,37). In addition, whereas iC3b is the canonical CR3 ligand, C3d deposition on erythrocytes facilitates their phagocytosis by monocytes in a metal ion- and CR3-dependent manner although C3d promotes phagocytosis much less efficiently than iC3b (30). The C3d-CR3 interaction even appears to have physiological relevance since C3dg mediated erythrophagocytosis may occur in individuals suffering from paroxysmal nocturnal hemoglobinuria (37), and may be involved in antigen-handover in the lymph nodes (29). In contrast CR4, a second integrin complement receptor which also binds iC3b, appears to have its primary binding site located within iC3b domains MG3 and MG4 (2). Here, we also demonstrate that the single cleaved $iC3b_1$ is a functional ligand for the CR3 headpiece with an affinity close to that of the double cleaved iC3b. Although this finding is of fundamental interest and supports a recent structure based model for two consecutive FI cleavages (3), the lifetime of $iC3b_1$ *in vivo* is unlikely to be long enough to make its interaction with CR3 relevant.

However, other regions in CR3 beside the α_M I-domain must contribute to iC3b binding, since its deletion leaves residual iC3b affinity in CR3 (31). Both the α_M β-propeller and the β_2 I-like domain have been suggested to be implicated in the interaction with iC3b (33,38,39), and on the iC3b side, mutations in the iC3b Nt-α' region associating with the MG7 domain weaken the iC3b-CR3 interaction (32). All these prior lines of evidence are consistent with the higher affinity of the CR3 headpiece for iC3b, as we now show by quantitating the interaction with a K_D of 30 nM in Mg^{2+}/Ca^{2+} as compared to 515 nM for the iC3b-α_MI interaction. To our knowledge, this is the highest

monovalent affinity measured between C3b, iC3b, C3dg and their five complement receptors.

Our solution scattering data bear witness of a compact particle with a maximum extent of 23 nm whereas the EM study featured a family of rather open CR3-iC3b complexes (2). The maximum extent of the iC3b-CR3 complex observed in the EM 2D classes is actually compatible with the 23 nm we observe by SAXS, whereas the open appearance of the complex present in the 2D classes presented in (2) appears to conflict with the pair distance distribution for the iC3b-CR3 complex obtained from solution scattering that we present here. This discrepancy may be due to partial dissociation of the complex during EM grid preparation, also in our hands negative stain EM grids with sample prepared as for our SAXS investigation do not present compact particles containing the complex despite extensive efforts and the use of gradient fixation (40). Further stabilization of the complex appears to be required to capture the compact complex we observe in solution on grids for electron microscopy.

With proper partial input models it is often possible to use rigid body modelling to obtain a structure for which the predicted scattering curve fits well to the experimental SAXS data (41). We have previously successfully fitted even the large and intricate C1 complex from the classical pathway of complement and the eye shaped properdin monomer with this approach (42,43). Although these conditions appear to be satisfied here with structures of C3c, the C3d-α_MI complex, homology models of CR3 based on CR4, we are still unable to obtain a satisfying fit to the experimental data. One reason could be the remnants of the CUB domain that after release of the 17 residues in C3f (Supplementary Fig 2A), which comprise roughly 100 residues. This degraded CUB domain is presumably more or less disordered and therefore difficult to model even though it constitutes only 11 kDa out of the 320 kDa iC3b-CR3 headpiece complex. A collapsed structure of the CUB domain in iC3b is supported by the great variation in the position of the thioester domain observed by negative stain EM (2,3). Furthermore, it remains an option that the iC3b/CR3 complex despite the compact appearance suggested by *ab initio* modelling actually exists as an ensemble of conformations maintained by the defined MIDAS dependent interaction between CR3 and the iC3b TE domain, aided by loose dynamic interactions between the CR3 and additional iC3b regions. Furthermore, regions outside of the CR3 headpiece are possibly required to obtain the full picture of the CR3-iC3b interaction. With respect to methods, single particle EM and crystallography may not be optimal, and cryo electron tomography investigations of *in vivo* like interfaces between a macrophage and an iC3b opsonized activator may be required to truly understand CR3-iC3b interaction at the structural levels.

Therapeutic intervention aiming at preventing specific CR3-ligand interactions has been investigated for decades, but is complicated by the plethora of structurally diverse CR3 ligands reported. Numerous CR3 function blocking antibodies are known, e.g. (44-46) and small molecules known as leukadherins binding CR3 and suppressing outside-in signaling upon ligand binding reduce inflammation and suppress tumor growth in animal models of cancer (47,48). Recent developments in research on neurobiology and neurodegenerative disease are likely to fuel the interest for a CR3 inhibitor. During development, activation of the classical pathway of complement on weakly signaling synapses leads to deposition of complement C3. Its degradation product iC3b is recognized by CR3-expressing microglia which phagocytize the iC3b opsonized synapses (6,7,49). Very recently, microglia CR3 was shown to support complement-dependent synapse elimination by microglia as a mechanism underlying the forgetting of remote memories (50). However, the same pathway that ensures correct development and removal of remote memories by pruning excess synapses, seems to be involved in neurodegenerative conditions like Alzheimer´s disease (11), frontotemporal dementia (FTD) (49) and spinal muscular atrophy (51). Our demonstration of a stable and compact complex between iC3b and the CR3 headpiece with a dissociation constant in the low nanomolar range should promote development of molecules aiming at specifically interfering with the iC3b/CR3

interaction while potentially preserving the ability of CR3 to recognize its many other ligands.

Experimental Procedures

Generation of a stable cell line expressing the CR3 headpiece fragment

The coding sequence of the human CR3 α_M-chain residues 17-773 containing the glycan knockout mutations N225R/N680R and β_2-chain residues 23-504 were cloned into the pIRES2-EGFP based in-house vectors ET10c and ET10b respectively. The ET10c vector contains a Human Rhinovirus (HRV) 3C protease recognition site, an acid coiled-coil region, a StrepII-tag and a His_6-tag on the 3', directly in-frame with the cloning site. The open reading frame was subsequently subcloned into pcDNA3.1(+). The ET10b vector contains an HRV 3C protease recognition site, a basic coiled-coil region, and a His_6-tag directly in-frame with the cloning site. The CR3 α_M- and β_2-chain were co-transfected into human embryonic kidney (HEK) 293S GnTi$^-$ cells (ATCC). The selection antibiotics Hygromycin B and G418 at 200 µg/mL and 1g/mL, respectively, were added to the cultures 48 hours post transfection. After selection the cells were assessed for GFP expression using fluorescence-activated cell sorting, and the top 5 % expressing clones were seeded in a 96 well cell culture plate. A final selection step was performed on the cell supernatants using sandwich ELISA by capturing the CR3 headpiece by use of an anti-CR3 α_M-chain antibody (CBRM 1/2), and detected using a biotinylated anti-CR3 β_2-chain antibody (IB4).

Expression and purification of the CR3 headpiece fragment

The CR3 headpiece stably transfected HEK293S cells were kept as adhesion cell culture growing in Dulbecco's Modification of Eagle's Medium (DMEM) GlutaMAX (Gibco) supplemented with 10 % (v/v) fetal bovine serum (FBS), 20 mM HEPES pH 7.5, 1 % Penicillin-Streptomycin (Gibco), 200 µg/mL Hygromycin B (Sigma-Aldrich) and 200 µg/mL G418 (Sigma-Aldrich). Before large scale purification, the cells were adapted to serum-free medium. The cell supernatant was harvested by centrifugation and subsequently filtered through 0.2 µm filters. The cleared cell supernatant was supplemented with 50 mM TRIS pH 8, 500 mM NaCl, 5 mM $MgCl_2$ and 1 mM $CaCl_2$ and applied to a 5 mL HisTrap Excel (GE Healthcare). Afterwards the column was washed with 40 mL of 20 mM TRIS pH 8, 1.5 M NaCl, 5 mM $MgCl_2$, 1 mM $CaCl_2$ and the protein was eluted in 20 mL of 20 mM TRIS pH 8, 150 mM NaCl, 5 mM $MgCl_2$, 1 mM $CaCl_2$, 400 mM imidazole. The elution was applied to a 1 mL StrepTactin column (GE Healthcare) equilibrated in 20 mM HEPES pH 7.5, 150 mM NaCl, 5 mM $MgCl_2$, 1 mM $CaCl_2$. The column was washed in 20 mM HEPES pH 7.5, 150 mM NaCl, 5 mM $MgCl_2$, 1 mM $CaCl_2$ and the protein was subsequently eluted in 20 mM HEPES pH 7.5, 150 mM NaCl, 5 mM $MgCl_2$, 1 mM $CaCl_2$, 2.5 mM D-desthiobiotin. 3C rhinovirus protease was added in a 1:10 mass ratio to CR3 and the reaction was allowed to proceed at 4°C overnight. A final polishing step was performed by size exclusion chromatography (SEC) on a 24 mL Superdex 200 increase (GE Healthcare) equilibrated in 20 mM HEPES pH 7.5, 150 mM NaCl, 5 mM $MgCl_2$ and 1 mM $CaCl_2$.

Cloning and Site-directed mutagenesis

A pET vector econding the vaccinia virus complement control protein (VCP) was kindly provided by Dr. Arvind Sahu, National Centre for Cell Science, Pune, India. It was subcloned into pETM-11 (EMBL) using the forward primer 5'-tttccatggggtgctgtactattccgtcacg-3' and the reverse primer 5'- tttggtaccctagcgtacacattttggaagttcc-3' with the restriction sites KpnI and NcoI. A site directed mutagenesis was performed on VCP in pETM-11 to form the C1S mutant by using the Quickchange Lightning Kit (Agilent Technologies) and the primers 5'-gcgccatggggtcctgtactattcc-3' and 5'-ggaatagtacaggaccccatggcgc-3'. The coding sequence including the C1S mutations was then subcloned into PcDNA3.1(+) using the forward primer 5'-aaagctagccaccatgaaggtggagagcgtgacgttcctgacattgttgcggaataggatgcgttctatcatcc-3' including the

secretion signal and the reverse primer 5'-acctctagactagtgatggtgatggtgatggcgtacacattttggaagttc-3'.

Protein production

Human CR3 α_MI-domain and C3d was expressed and purified as described in (29). C3b and iC3b was generated and purified as described in (34). hC3Nb1 was expressed and purified as described in (34). VCP was expressed by PEI transfection of HEK293F cells (Invitrogen). After expression, the cell supernatant was cleared by centrifugation followed by filtration through a 0.2 µm filter. The cleared supernatant was loaded on a 1 mL HisTrap Excel equilibrated in 20 mM TRIS pH 8.5, 500 mM NaCl. The column was subsequently washed in 10 mL of 20 mM TRIS pH 8.5, 500 mM NaCl and eluted in 5 mL of 20 mM TRIS pH 8.5, 500 mM NaCl, 200 mM Imidazole. The elution was diluted ten-fold and loaded on a 1 mL HisTrap Crude equilibrated in 20 mM TRIS pH 8.5, 500 mM NaCl, 35 mM Imidazole. The column was then washed in 10 mL of 20 mM TRIS pH 8.5, 500 mM NaCl, 35 mM Imidazole, and VCP was eluted in 2 mL of 20 mM TRIS pH 8.5, 500 mM NaCl, 250 mM Imidazole. The protein was diluted against 20 mM HEPES pH 7.5, 250 mM NaCl. iC3b$_1$ was generated by mixing of C3b with 100 % (w/v) VCP, 0.5 % (w/v) FI and was incubation for 30 minutes at 37°C after which FI was inhibited by addition of 2 mM Benzamidine and 1 mM Pefabloc SC. The cleaved C3b was applied to a 1 mL MonoQ (GE Healthcare) equilibrated in 20 mM HEPES pH 7.5, 150 mM NaCl. The column was washed in 20 mM HEPES pH 7.5, 170 mM NaCl before being eluted by a 30 mL linear gradient from 170-210 mM NaCl. The fraction containing pure iC3b$_1$ without contamination of C3b or iC3b was pooled and concentrated before being applied to a 24 mL Superdex 200 increase equilibrated in 20 mM HEPES pH 7.5, 150 mM NaCl.

Analytical SEC analysis

For analyzing the effect of different divalent cations on the oligomeric state of CR3, 50 µL of CR3 headpiece at 2 µg/µL was diluted four-fold in either 20 mM HEPES pH 7.5, 150 mM NaCl, 1 mM $MnCl_2$, 0.2 mM $CaCl_2$; 20 mM HEPES pH 7.5, 150 mM NaCl, 5 mM $MgCl_2$, 1 mM $CaCl_2$; or 20 mM HEPES pH 7.5, 150 mM NaCl, 5 mM $NiCl_2$, 1 mM $CaCl_2$. The protein was incubated for 1 hour at room temperature before being injected on a 24 mL Superdex 200 increase equilibrated in the respective protein dilution buffer. For analyzing the complex formation between CR3 and iC3b, 15 µg of iC3b was mixed with 1.1 fold molar excess of CR3. The sample was injected on a 2.4 mL Superdex 200 increase equilibrated in 20 mM HEPES pH 7.5, 150 mM NaCl, 5 mM $MgCl_2$, 1 mM $CaCl_2$. Control experiments injecting either CR3 or iC3b in the same amount was also performed. The experiment was repeated on the same column in 20 mM HEPES pH 7.5, 150 mM NaCl, 1 mM $MnCl_2$, 0.2 mM $CaCl_2$. For analyzing the complex formation between CR3 and iC3b$_1$, the CR3 headpiece was mixed with two-fold molar excess of iC3b$_1$ and was incubated for 15 minutes at room temperature. The complex was applied to a Superdex 200 increase equilibrated in 20 mM HEPES pH 7.5, 150 mM NaCl, 5 mM $MgCl_2$ and 1 mM $CaCl_2$. iC3b$_1$ was applied to a 24 mL Superdex 200 increase equilibrated in 20 mM HEPES pH 7.5, 150 mM NaCl, 5 mM $MgCl_2$ and 1 mM $CaCl_2$.

SAXS analysis of the CR3 headpiece, C3b, iC3b and iC3b$_1$.

SAXS measurements of CR3 headpiece, C3b, iC3b$_1$ and iC3b were performed in batch mode at the P12 beamline at PETRA III, Hamburg, Germany (52). The data were collected in a temperature-controlled capillary at 20ºC using a PILATUS 2M pixel detector (DECTRIS) with λ = 1.240 Å. The sample-to-detector distance was 3.0 m covering $0.002 < q < 0.48$ Å^{-1} ($q=4\pi\cdot\sin\theta\cdot\lambda^{-1}$, where 2θ is the scattering angle). Samples of CR3 were prepared at 0.7, 1.3, 1.7 and 2.9 mg/mL, samples of C3b, iC3b or iC3b$_1$ were prepared at 7.3, 13.0, and 8.0 mg/mL respectively, where after data was collected with twenty exposures of 45 ms. Radial averaging, buffer subtraction and concentration scaling was performed by the automated pipeline at the beamline (53) and the pair

distribution function was calculated by indirect Fourier transformation using GNOM (54). In-line SEC-SAXS data for the CR3 headpiece in complex with iC3b and C3d were likewise collected at the P12 beamline at PETRA III. Scattering was recorded from the elution of a 24 mL Superdex 200 increase equilibrated in 20 mM HEPES pH 7.5, 150 mM NaCl with a flow rate of 0.25 mL/min. The CR3 headpiece was mixed with 20 % molar excess of iC3b or 4 fold molar excess of C3d and injected on the SEC column. Each frame during the SEC-SAXS run covers a 0.955 s exposure performed every second. Normalization and radial averaging was performed at the beamline using the automated pipeline (52,55). For buffer subtraction the best buffer scattering was determined by averaging every tenth frame before the void of the SEC column. The goodness-of-fit test known as correlation map was used to verify that the scattering profiles in the bins were not statistically different (56). Each of the averaged buffer frames were then compared to each other using correlation map, and the similar frames were averaged. Buffer subtraction was performed for all protein containing frames. Every ten frames were averaged if they were not statistically different. The averages were then compared using correlation map and the similar frames were averaged. The pair-distribution function was calculated by indirect Fourier transform using GNOM (54). Ab intio models were generated using dammif, and subsequently clustered using damclust (41).

Surface plasmon resonance assays.

The experiments were performed on a Biacore T200 instrument with a running buffer containing 20 mM HEPES pH 7.5, 150 mM NaCl, 5 mM $MgCl_2$, 1 mM $CaCl_2$ unless otherwise stated. Streptavidin was immobilized on a CMD500M chip (XanTec Bioanalytics) to 200 response units. C3d, iC3b, or $iC3b_1$ biotinylated on the thioester cysteine was injected on the chip until the surface was saturated. For the kinetics experiments using iC3b or $iC3b_1$, the CR3 headpiece was injected in a concentration series ranging from 0.3215 nM to 100 nM, whereas for C3d, the CR3 headpiece was injected in a concentration series ranging from 3.25 nM to 2000 nM. The surface was regenerated by using a buffer containing 50 mM EDTA, 1 M NaCl, 100 mM HEPES pH 7.5. The data were analyzed using a 1:1 binding model, and the reported on- and off-rates are averages of three independent experiments. The kinetic experiment with iC3b on the surface was repeated three times in the buffer containing 20 mM HEPES pH 7.5, 150 mM NaCl, 1 mM $MnCl_2$, 0.2 mM $CaCl_2$ as well. The competition assays were performed on the iC3b surface where 20 mM of CR3 headpiece was injected either alone, or pre-incubated on ice for 1 hour with 10, 20, 50, 100, 200, or 1000 nM of iC3b, C3d or C3b respectively. All experiments were performed in triplicates.

Single particle negative stain EM analysis

Carbon-evaporated copper grids (G400-C3, Gilder) were glow-discharged for 45 seconds at 25 mA using an easiGlow (PELCO). Three µL of CR3 headpiece at 13 µg/mL was adsorbed to the grid for 5 seconds before being blotted away. The grid was washed twice in 3 µL of the 20 mM HEPES pH 7.5, 150 mM NaCl followed by a staining step using a 3 µL drop of 2 % (w/v) uranyl formate allowing it to stain the grid for 45 seconds. The grids were imaged on a 120 kV Tecnai G2 spirit. Automated data collection was performed at a nominal magnification of 67.000x and a defocus ranging from -0.7 to -1.7 µm using the leginon software (57). Particles were picked using DoG picker (58) in the Appion framework (59). 2D classification, Initial model generation using SGD, and 3D classification was performed in RELION (60).

Crystallization and crystal structure determination of $iC3b_1$ in complex with hC3Nb1

Crystals of the $iC3b_1$ – hC3Nb1 complex were grown at 19°C in sitting drops made by mixing the complex at 7.5 mg/mL in a 1:1 ratio with reservoir solution containing 96 mM Bis-TRIS Propane pH 8.5, 4 mM Bis-TRIS Propane pH 7, 6.5 % (w/v) PEG 20.000. Crystals were cryo-protected by soaking in reservoir solution supplemented with 32.5 % PEG400 prior to flash cooling in liquid

nitrogen. Data were collected at the European synchrotron radiation facility (Grenoble, France) beamline ID23-2 with λ=0.873127 Å at 100 K and processed with XDS (61). The structure was determined using the coordinates of the C3b – hC3Nb1 complex (RCSB entry 6EHG) with the C345c, CUB and TE domain removed for molecular replacement in Phaser (62). The initial map was used for manual placement of the C345c, TE and CUB domains in Coot (63) followed by one round of rigid body refinement, grouped B-factors and TLS groups in phenix.refine (64).

Data availability: The crystal structure presented in this paper has been deposited in the Protein Data Bank (PDB) with the following code: 6YO6.

Acknowledgements

We thank the staff at ID23-2 beamline at ESRF and the P12 beamline at PETRAIII for help during data collection. We thank Dr. Arvind Sahu for providing a plasmid containing the coding sequence of VCP. The authors would like to acknowledge Christine Schar for assistance with SPR and Karen Margrethe Nielsen for technical support.

Funding and additional information: This work was supported by the Lundbeck Foundation (BRAINSTRUC, grant no. R155-2015-2666) and the Danish Foundation for Independent Research (grant no 4181-00137).

Conflict of interest: The authors declare no conflicts of interest in regards to this manuscript.

References

1. Zipfel, P. F., and Skerka, C. (2009) Complement regulators and inhibitory proteins. *Nat Rev Immunol* **9**, 729-740
2. Xu, S., Wang, J., Wang, J. H., and Springer, T. A. (2017) Distinct recognition of complement iC3b by integrins alphaXbeta2 and alphaMbeta2. *Proc Natl Acad Sci U S A* **114**, 3403-3408
3. Xue, X. G., Wu, J., Ricklin, D., Forneris, F., Di Crescenzio, P., Schmidt, C. Q., Granneman, J., Sharp, T. H., Lambris, J. D., and Gros, P. (2017) Regulator-dependent mechanisms of C3b processing by factor I allow differentiation of immune responses. *Nat Struct Mol Biol* **24**, 643-+
4. Vorup-Jensen, T., and Jensen, R. K. (2018) Structural Immunology of Complement Receptors 3 and 4. *Front Immunol* **9**, 2716
5. Erdei, A., Lukacsi, S., Macsik-Valent, B., Nagy-Balo, Z., Kurucz, I., and Bajtay, Z. (2019) Non-identical twins: Different faces of CR3 and CR4 in myeloid and lymphoid cells of mice and men. *Semin Cell Dev Biol* **85**, 110-121
6. Stevens, B., Allen, N. J., Vazquez, L. E., Howell, G. R., Christopherson, K. S., Nouri, N., Micheva, K. D., Mehalow, A. K., Huberman, A. D., Stafford, B., Sher, A., Litke, A. M., Lambris, J. D., Smith, S. J., John, S. W., and Barres, B. A. (2007) The classical complement cascade mediates CNS synapse elimination. *Cell* **131**, 1164-1178
7. Schafer, D. P., Lehrman, E. K., Kautzman, A. G., Koyama, R., Mardinly, A. R., Yamasaki, R., Ransohoff, R. M., Greenberg, M. E., Barres, B. A., and Stevens, B. (2012) Microglia sculpt postnatal neural circuits in an activity and complement-dependent manner. *Neuron* **74**, 691-705
8. Wakselman, S., Bechade, C., Roumier, A., Bernard, D., Triller, A., and Bessis, A. (2008) Developmental neuronal death in hippocampus requires the microglial CD11b integrin and DAP12 immunoreceptor. *J Neurosci* **28**, 8138-8143
9. Jiang, L., Chen, S. H., Chu, C. H., Wang, S. J., Oyarzabal, E., Wilson, B., Sanders, V., Xie, K., Wang, Q., and Hong, J. S. (2015) A novel role of microglial NADPH oxidase in mediating extra-synaptic function of norepinephrine in regulating brain immune homeostasis. *Glia* **63**, 1057-1072
10. Kadioglu, A., De Filippo, K., Bangert, M., Fernandes, V. E., Richards, L., Jones, K., Andrew, P. W., and Hogg, N. (2011) The integrins Mac-1 and alpha4beta1 perform crucial roles in neutrophil and T cell recruitment to lungs during Streptococcus pneumoniae infection. *J Immunol* **186**, 5907-5915
11. Hong, S., Beja-Glasser, V. F., Nfonoyim, B. M., Frouin, A., Li, S., Ramakrishnan, S., Merry, K. M., Shi, Q., Rosenthal, A., Barres, B. A., Lemere, C. A., Selkoe, D. J., and Stevens, B. (2016) Complement and microglia mediate early synapse loss in Alzheimer mouse models. *Science* **352**, 712-716
12. Luo, B. H., and Springer, T. A. (2006) Integrin structures and conformational signaling. *Curr Opin Cell Biol* **18**, 579-586
13. Springer, T. A., and Dustin, M. L. (2012) Integrin inside-out signaling and the immunological synapse. *Curr Opin Cell Biol* **24**, 107-115

14. Vorup-Jensen, T. (2012) On the roles of polyvalent binding in immune recognition: perspectives in the nanoscience of immunology and the immune response to nanomedicines. *Adv Drug Deliv Rev* **64**, 1759-1781
15. Diamond, M. S., Garcia-Aguilar, J., Bickford, J. K., Corbi, A. L., and Springer, T. A. (1993) The I domain is a major recognition site on the leukocyte integrin Mac-1 (CD11b/CD18) for four distinct adhesion ligands. *J Cell Biol* **120**, 1031-1043
16. Chavakis, T., Bierhaus, A., Al-Fakhri, N., Schneider, D., Witte, S., Linn, T., Nagashima, M., Morser, J., Arnold, B., Preissner, K. T., and Nawroth, P. P. (2003) The pattern recognition receptor (RAGE) is a counterreceptor for leukocyte integrins: a novel pathway for inflammatory cell recruitment. *J Exp Med* **198**, 1507-1515
17. Lishko, V. K., Yakubenko, V. P., Ugarova, T. P., and Podolnikova, N. P. (2018) Leukocyte integrin Mac-1 (CD11b/CD18, alphaMbeta2, CR3) acts as a functional receptor for platelet factor 4. *J Biol Chem* **293**, 6869-6882
18. Liu, Y. S., Wang, L. F., Cheng, X. S., Huo, Y. N., Ouyang, X. M., Liang, L. Y., Lin, Y., Wu, J. F., Ren, J. L., and Guleng, B. (2019) The pattern-recognition molecule mindin binds integrin Mac-1 to promote macrophage phagocytosis via Syk activation and NF-kappaB p65 translocation. *J Cell Mol Med* **23**, 3402-3416
19. Morgan, J., Saleem, M., Ng, R., Armstrong, C., Wong, S. S., Caulton, S. G., Fickling, A., Williams, H. E. L., Munday, A. D., Lopez, J. A., Searle, M. S., and Emsley, J. (2019) Structural basis of the leukocyte integrin Mac-1 I-domain interactions with the platelet glycoprotein Ib. *Blood Adv* **3**, 1450-1459
20. Saggu, G., Okubo, K., Chen, Y., Vattepu, R., Tsuboi, N., Rosetti, F., Cullere, X., Washburn, N., Tahir, S., Rosado, A. M., Holland, S. M., Anthony, R. M., Sen, M., Zhu, C., and Mayadas, T. N. (2018) Cis interaction between sialylated FcgammaRIIA and the alphaI-domain of Mac-1 limits antibody-mediated neutrophil recruitment. *Nat Commun* **9**, 5058
21. Wolf, D., Hohmann, J. D., Wiedemann, A., Bledzka, K., Blankenbach, H., Marchini, T., Gutte, K., Zeschky, K., Bassler, N., Hoppe, N., Rodriguez, A. O., Herr, N., Hilgendorf, I., Stachon, P., Willecke, F., Duerschmied, D., von zur Muhlen, C., Soloviev, D. A., Zhang, L., Bode, C., Plow, E. F., Libby, P., Peter, K., and Zirlik, A. (2011) Binding of CD40L to Mac-1's I-domain involves the EQLKKSKTL motif and mediates leukocyte recruitment and atherosclerosis--but does not affect immunity and thrombosis in mice. *Circ Res* **109**, 1269-1279
22. Zhang, X., Bajic, G., Andersen, G. R., Christiansen, S. H., and Vorup-Jensen, T. (2016) The cationic peptide LL-37 binds Mac-1 (CD11b/CD18) with a low dissociation rate and promotes phagocytosis. *Biochim Biophys Acta* **1864**, 471-478
23. DuMont, A. L., Yoong, P., Day, C. J., Alonzo, F., 3rd, McDonald, W. H., Jennings, M. P., and Torres, V. J. (2013) Staphylococcus aureus LukAB cytotoxin kills human neutrophils by targeting the CD11b subunit of the integrin Mac-1. *Proc Natl Acad Sci U S A* **110**, 10794-10799
24. Ranganathan, S., Cao, C., Catania, J., Migliorini, M., Zhang, L., and Strickland, D. K. (2011) Molecular basis for the interaction of low density lipoprotein receptor-related protein 1 (LRP1) with integrin alphaMbeta2: identification of binding sites within alphaMbeta2 for LRP1. *J Biol Chem* **286**, 30535-30541
25. Lee, J. O., Rieu, P., Arnaout, M. A., and Liddington, R. (1995) Crystal structure of the A domain from the alpha subunit of integrin CR3 (CD11b/CD18). *Cell* **80**, 631-638
26. Lee, J. O., Bankston, L. A., Arnaout, M. A., and Liddington, R. C. (1995) Two conformations of the integrin A-domain (I-domain): a pathway for activation? *Structure* **3**, 1333-1340
27. Xiao, T., Takagi, J., Coller, B. S., Wang, J. H., and Springer, T. A. (2004) Structural basis for allostery in integrins and binding to fibrinogen-mimetic therapeutics. *Nature* **432**, 59-67

28. Zhang, K., and Chen, J. (2012) The regulation of integrin function by divalent cations. *Cell Adh Migr* **6**, 20-29
29. Bajic, G., Yatime, L., Sim, R. B., Vorup-Jensen, T., and Andersen, G. R. (2013) Structural insight on the recognition of surface-bound opsonins by the integrin I domain of complement receptor 3. *Proc Natl Acad Sci U S A* **110**, 16426-16431
30. Gaither, T. A., Vargas, I., Inada, S., and Frank, M. M. (1987) The complement fragment C3d facilitates phagocytosis by monocytes. *Immunology* **62**, 405-411
31. Yalamanchili, P., Lu, C., Oxvig, C., and Springer, T. A. (2000) Folding and function of I domain-deleted Mac-1 and lymphocyte function-associated antigen-1. *J Biol Chem* **275**, 21877-21882
32. Taniguchi-Sidle, A., and Isenman, D. E. (1994) Interactions of human complement component C3 with factor B and with complement receptors type 1 (CR1, CD35) and type 3 (CR3, CD11b/CD18) involve an acidic sequence at the N-terminus of C3 alpha'-chain. *J Immunol* **153**, 5285-5302
33. Li, Y., and Zhang, L. (2003) The fourth blade within the beta-propeller is involved specifically in C3bi recognition by integrin alpha M beta 2. *J Biol Chem* **278**, 34395-34402
34. Jensen, R. K., Pihl, R., Gadeberg, T. A. F., Jensen, J. K., Andersen, K. R., Thiel, S., Laursen, N. S., and Andersen, G. R. (2018) A potent complement factor C3-specific nanobody inhibiting multiple functions in the alternative pathway of human and murine complement. *J Biol Chem* **293**, 6269-6281
35. Sahu, A., Isaacs, S. N., Soulika, A. M., and Lambris, J. D. (1998) Interaction of vaccinia virus complement control protein with human complement proteins: Factor I-mediated degradation of C3b to iC3b(1) inactivates the alternative complement pathway. *Journal of Immunology* **160**, 5596-5604
36. Michishita, M., Videm, V., and Arnaout, M. A. (1993) A novel divalent cation-binding site in the A domain of the beta 2 integrin CR3 (CD11b/CD18) is essential for ligand binding. *Cell* **72**, 857-867
37. Lin, Z., Schmidt, C. Q., Koutsogiannaki, S., Ricci, P., Risitano, A. M., Lambris, J. D., and Ricklin, D. (2015) Complement C3dg-mediated erythrophagocytosis: implications for paroxysmal nocturnal hemoglobinuria. *Blood* **126**, 891-894
38. MacPherson, M., Lek, H. S., Prescott, A., and Fagerholm, S. C. (2011) A systemic lupus erythematosus-associated R77H substitution in the CD11b chain of the Mac-1 integrin compromises leukocyte adhesion and phagocytosis. *The Journal of biological chemistry* **286**, 17303-17310
39. Xiong, Y.-M., Haas, T. a., and Zhang, L. (2002) Identification of functional segments within the beta2I-domain of integrin alphaMbeta2. *The Journal of biological chemistry* **277**, 46639-46644
40. Stark, H. (2010) GraFix: stabilization of fragile macromolecular complexes for single particle cryo-EM. *Methods Enzymol* **481**, 109-126
41. Petoukhov, M. V., Franke, D., Shkumatov, A. V., Tria, G., Kikhney, A. G., Gajda, M., Gorba, C., Mertens, H. D., Konarev, P. V., and Svergun, D. I. (2012) New developments in the ATSAS program package for small-angle scattering data analysis. *J Appl Crystallogr* **45**, 342-350
42. Pedersen, D. V., Roumenina, L., Jensen, R. K., Gadeberg, T. A., Marinozzi, C., Picard, C., Rybkine, T., Thiel, S., Sorensen, U. B., Stover, C., Fremeaux-Bacchi, V., and Andersen, G. R. (2017) Functional and structural insight into properdin control of complement alternative pathway amplification. *EMBO J* **36**, 1084-1099
43. Mortensen, S. A., Sander, B., Jensen, R. K., Pedersen, J. S., Golas, M. M., Jensenius, J. C., Hansen, A. G., Thiel, S., and Andersen, G. R. (2017) Structure and activation of C1, the complex initiating the classical pathway of the complement cascade. *Proc Natl Acad Sci U S A* **114**, 986-991
44. Oxvig, C., Lu, C., and Springer, T. A. (1999) Conformational changes in tertiary structure near the ligand binding site of an integrin I domain. *Proc Natl Acad Sci U S A* **96**, 2215-2220
45. Mahalingam, B., Ajroud, K., Alonso, J. L., Anand, S., Adair, B. D., Horenstein, A. L., Malavasi, F., Xiong, J. P., and Arnaout, M. A. (2011) Stable coordination of the inhibitory Ca2+ ion at the metal ion-dependent

adhesion site in integrin CD11b/CD18 by an antibody-derived ligand aspartate: implications for integrin regulation and structure-based drug design. *J Immunol* **187**, 6393-6401

46. Wolf, D., Anto-Michel, N., Blankenbach, H., Wiedemann, A., Buscher, K., Hohmann, J. D., Lim, B., Bauml, M., Marki, A., Mauler, M., Duerschmied, D., Fan, Z., Winkels, H., Sidler, D., Diehl, P., Zajonc, D. M., Hilgendorf, I., Stachon, P., Marchini, T., Willecke, F., Schell, M., Sommer, B., von Zur Muhlen, C., Reinohl, J., Gerhardt, T., Plow, E. F., Yakubenko, V., Libby, P., Bode, C., Ley, K., Peter, K., and Zirlik, A. (2018) A ligand-specific blockade of the integrin Mac-1 selectively targets pathologic inflammation while maintaining protective host-defense. *Nat Commun* **9**, 525
47. Schmid, M. C., Khan, S. Q., Kaneda, M. M., Pathria, P., Shepard, R., Louis, T. L., Anand, S., Woo, G., Leem, C., Faridi, M. H., Geraghty, T., Rajagopalan, A., Gupta, S., Ahmed, M., Vazquez-Padron, R. I., Cheresh, D. A., Gupta, V., and Varner, J. A. (2018) Integrin CD11b activation drives anti-tumor innate immunity. *Nat Commun* **9**, 5379
48. Maiguel, D., Faridi, M. H., Wei, C., Kuwano, Y., Balla, K. M., Hernandez, D., Barth, C. J., Lugo, G., Donnelly, M., Nayer, A., Moita, L. F., Schurer, S., Traver, D., Ruiz, P., Vazquez-Padron, R. I., Ley, K., Reiser, J., and Gupta, V. (2011) Small molecule-mediated activation of the integrin CD11b/CD18 reduces inflammatory disease. *Sci Signal* **4**, ra57
49. Lui, H., Zhang, J., Makinson, S. R., Cahill, M. K., Kelley, K. W., Huang, H. Y., Shang, Y., Oldham, M. C., Martens, L. H., Gao, F., Coppola, G., Sloan, S. A., Hsieh, C. L., Kim, C. C., Bigio, E. H., Weintraub, S., Mesulam, M. M., Rademakers, R., Mackenzie, I. R., Seeley, W. W., Karydas, A., Miller, B. L., Borroni, B., Ghidoni, R., Farese, R. V., Jr., Paz, J. T., Barres, B. A., and Huang, E. J. (2016) Progranulin Deficiency Promotes Circuit-Specific Synaptic Pruning by Microglia via Complement Activation. *Cell* **165**, 921-935
50. Wang, C., Yue, H., Hu, Z., Shen, Y., Ma, J., Li, J., Wang, X. D., Wang, L., Sun, B., Shi, P., Wang, L., and Gu, Y. (2020) Microglia mediate forgetting via complement-dependent synaptic elimination. *Science* **367**, 688-694
51. Vukojicic, A., Delestree, N., Fletcher, E. V., Pagiazitis, J. G., Sankaranarayanan, S., Yednock, T. A., Barres, B. A., and Mentis, G. Z. (2019) The Classical Complement Pathway Mediates Microglia-Dependent Remodeling of Spinal Motor Circuits during Development and in SMA. *Cell Rep* **29**, 3087-3100 e3087
52. Blanchet, C. E., Spilotros, A., Schwemmer, F., Graewert, M. A., Kikhney, A., Jeffries, C. M., Franke, D., Mark, D., Zengerle, R., Cipriani, F., Fiedler, S., Roessle, M., and Svergun, D. I. (2015) Versatile sample environments and automation for biological solution X-ray scattering experiments at the P12 beamline (PETRA III, DESY). *J Appl Crystallogr* **48**, 431-443
53. Franke, D., Kikhney, A. G., and Svergun, D. I. (2012) Automated acquisition and analysis of small angle X-ray scattering data. *Nucl Instrum Meth A* **689**, 52-59
54. Svergun, D. I. (1992) Determination of the Regularization Parameter in Indirect-Transform Methods Using Perceptual Criteria. *Journal of Applied Crystallography* **25**, 495-503
55. Graewert, M. A., Franke, D., Jeffries, C. M., Blanchet, C. E., Ruskule, D., Kuhle, K., Flieger, A., Schafer, B., Tartsch, B., Meijers, R., and Svergun, D. I. (2015) Automated pipeline for purification, biophysical and x-ray analysis of biomacromolecular solutions. *Sci Rep* **5**, 10734
56. Franke, D., Jeffries, C. M., and Svergun, D. I. (2015) Correlation Map, a goodness-of-fit test for one-dimensional X-ray scattering spectra. *Nat Methods* **12**, 419-422
57. Suloway, C., Pulokas, J., Fellmann, D., Cheng, A., Guerra, F., Quispe, J., Stagg, S., Potter, C. S., and Carragher, B. (2005) Automated molecular microscopy: the new Leginon system. *J Struct Biol* **151**, 41-60
58. Voss, N. R., Yoshioka, C. K., Radermacher, M., Potter, C. S., and Carragher, B. (2009) DoG Picker and TiltPicker: software tools to facilitate particle selection in single particle electron microscopy. *J Struct Biol* **166**, 205-213

59. Lander, G. C., Stagg, S. M., Voss, N. R., Cheng, A., Fellmann, D., Pulokas, J., Yoshioka, C., Irving, C., Mulder, A., Lau, P. W., Lyumkis, D., Potter, C. S., and Carragher, B. (2009) Appion: an integrated, database-driven pipeline to facilitate EM image processing. *J Struct Biol* **166**, 95-102
60. Scheres, S. H. (2012) RELION: implementation of a Bayesian approach to cryo-EM structure determination. *J Struct Biol* **180**, 519-530
61. Kabsch, W. (2010) Integration, scaling, space-group assignment and post-refinement. *Acta crystallographica. Section D, Biological crystallography* **66**, 133-144
62. McCoy, A. J., Grosse-Kunstleve, R. W., Adams, P. D., Winn, M. D., Storoni, L. C., and Read, R. J. (2007) Phaser crystallographic software. *J Appl Crystallogr* **40**, 658-674
63. Emsley, P., Lohkamp, B., Scott, W. G., and Cowtan, K. (2010) Features and development of Coot. *Acta crystallographica. Section D, Biological crystallography* **66**, 486-501
64. Afonine, P. V., Grosse-Kunstleve, R. W., Echols, N., Headd, J. J., Moriarty, N. W., Mustyakimov, M., Terwilliger, T. C., Urzhumtsev, A., Zwart, P. H., and Adams, P. D. (2012) Towards automated crystallographic structure refinement with phenix.refine. *Acta crystallographica. Section D, Biological crystallography* **68**, 352-367

Table 1. Summary of SPR analysis of the CR3 headpiece interaction with various C3 fragments. The on- and off-rates are shown as average values of three independent experiments ± the standard deviation. For C3d steady-state analysis was performed to calculate the dissociation constant, which was obtained by non-linear regression against the average binding response of three independent experiments, and the K_D is reported ± the standard deviation of the fit.

	k_{on} (M^{-1} s^{-1})	k_{off} (s^{-1})	K_D (nM)
iC3b (Mg^{2+})	$1.22 \cdot 10^6 \pm 0.44 \cdot 10^6$	$3.60 \cdot 10^{-2} \pm 0.035 \cdot 10^{-2}$	29.6
iC3b (Mn^{2+})	$1.95 \cdot 10^5 \pm 0.029 \cdot 10^5$	$1.21 \cdot 10^{-3} \pm 0.016 \cdot 10^{-3}$	6.17
C3d (Mg^{2+})	N/A	N/A	515 ± 33.8
iC3b$_1$ (Mg^{2+})	$6.71 \cdot 10^5 \pm 0.25 \cdot 10^5$	$6.40 \cdot 10^{-2} \pm 0.013 \cdot 10^{-2}$	50.7

Figures

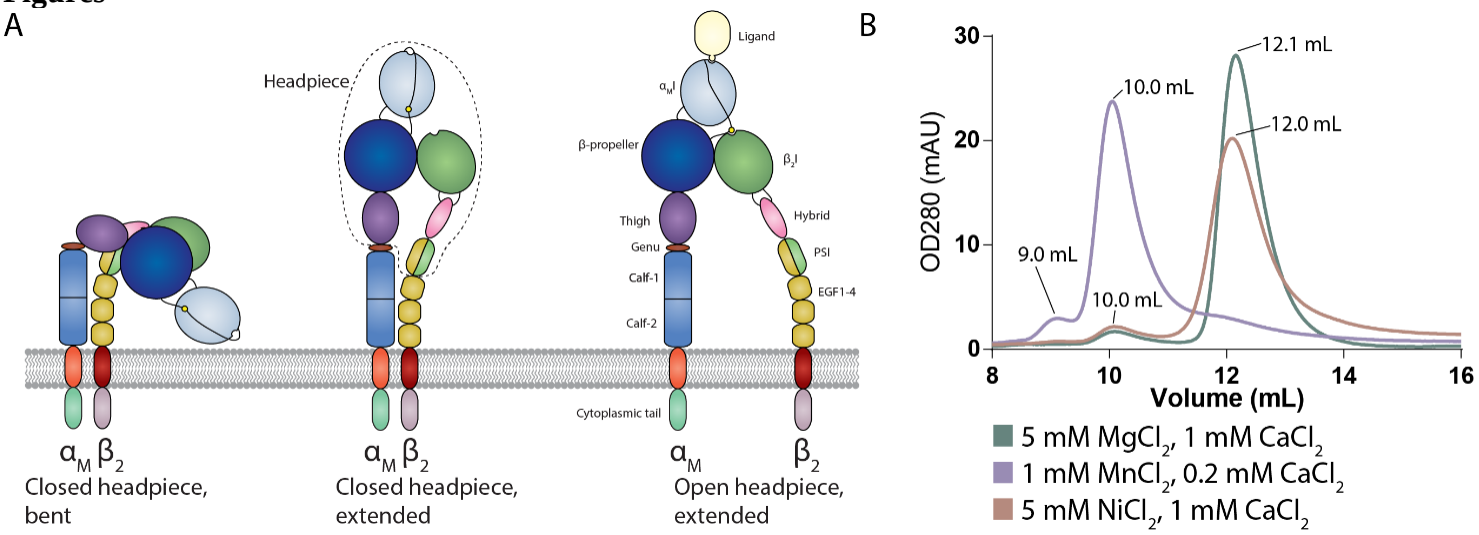

Figure 1. Characterization of the CR3 headpiece fragment. A. Domain arrangement and structural states of CR3. The bent conformation is a low affinity conformation. The integrin can also exist in an intermediary affinity conformation where it extends outward from the cell membrane. The highest affinity conformation is obtained when the headpiece opens, allowing ligand binding and signalling to occur. The domains making up the headpiece is indicated by a dotted line **B.** Comparison of analytical SEC runs with the CR3 headpiece fragment in $MgCl_2$ (turquoise), $MnCl_2$ (purple), and $NiCl_2$ (brown), revealing the cation dependence of CR3 headpiece oligomerization.

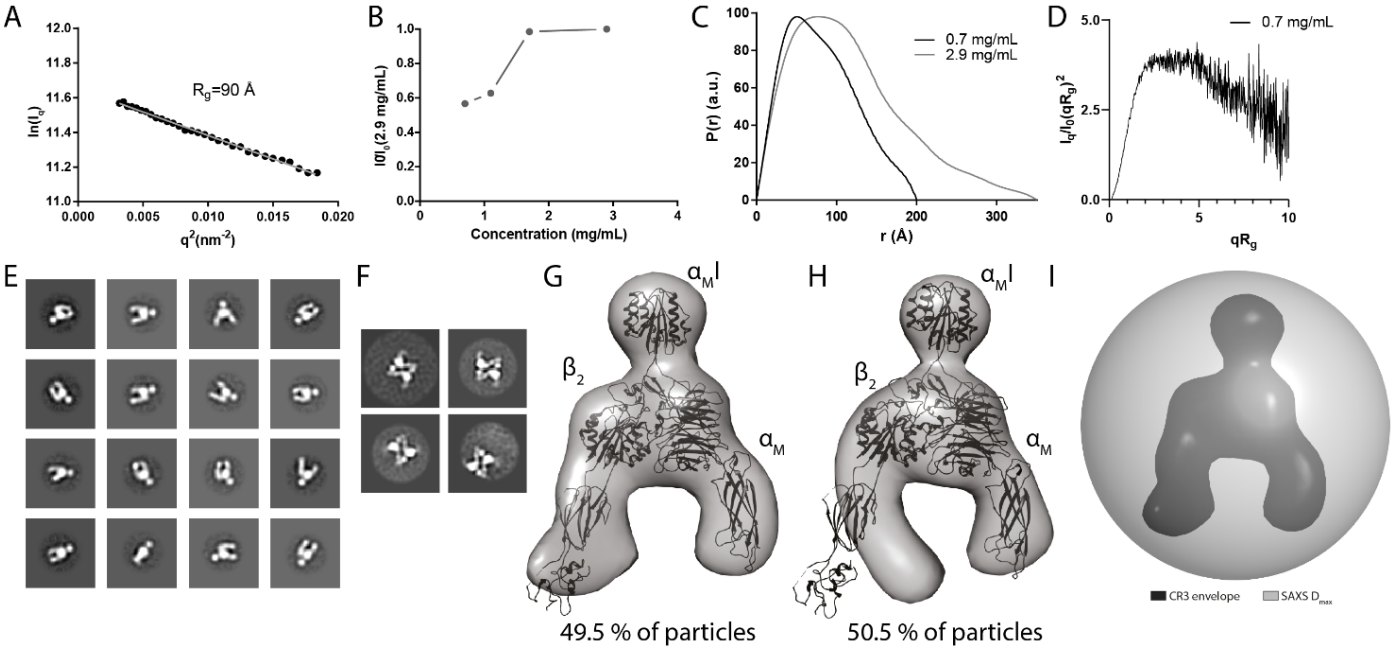

Figure 2. Structural characterization of the CR3 headpiece fragment. A. Guinier analysis of the CR3 headpiece SAXS data at 2.9 mg/mL. **B.** The forward scattering of CR3 is plotted as a function of concentration, indicating that CR3 undergoes dimerization at higher concentrations. **C. P**air distribution functions of CR3 headpiece at either 0.7 mg/mL (black) or 2.9 mg/mL (grey) showing that D_{max} increases from ~200 to 350 Å at higher concentrations. **D.** The Guiner normalized Kratky plot of the CR3 headpiece at 2.9 mg/mL showing that CR3 is an ordered protein with a high degree of flexibility. **E.** The 2D class averages of negatively stained CR3 headpiece from the 16 highest abundance 2D classes, showing that CR3 mainly exists as a monomer in both the open and closed conformation. **F.** EM 2D class averages of the minor fraction of CR3 present as dimer. **G.-H.** 3D reconstructions of the CR3 headpiece fragment in either the open (**G**) or closed (**H**) conformation. **I.** Comparison of the 3D reconstruction of CR3 headpiece in the open conformation (black) and the D_{max} obtained in SAXS indicated as a grey sphere with a diameter equal to D_{max}.

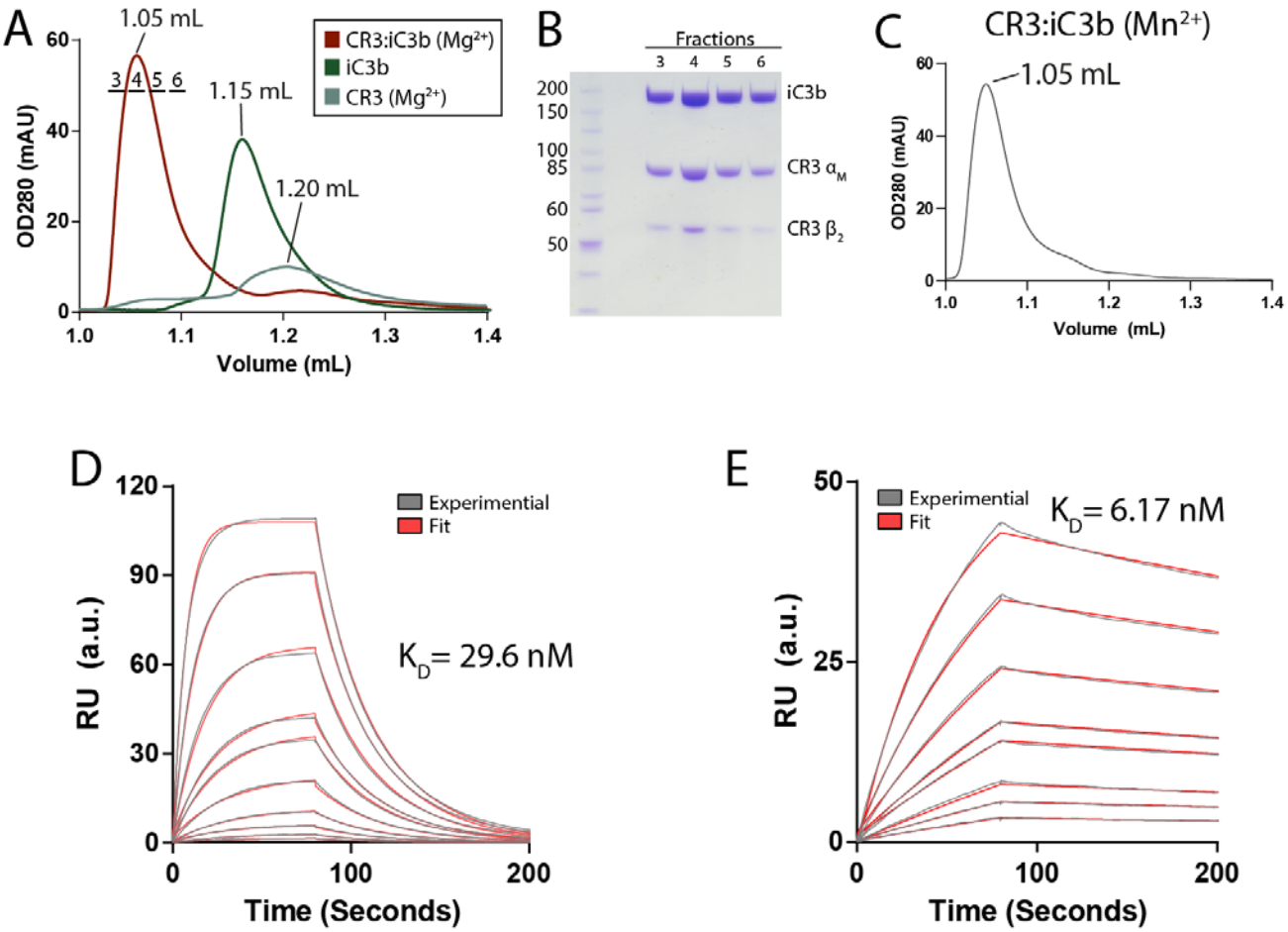

Figure 3. Analysis of the CR3:iC3b interaction. A. SEC analysis of the complex formation between CR3 and iC3b in the buffer containing 5 mM $MgCl_2$, 1 mM $CaCl_2$. The elution profile of the CR3:iC3b, iC3b and CR3 headpiece is shown in red, green and turquoise respectively. A significant shift in elution volume can be seen between the complex and both iC3b and CR3 alone. **B.** Non-reducing SDS-PAGE analysis of the fractions indicated in panel **A**, both the iC3b and CR3 bands can be identified. **C.** SEC chromatogram of the CR3:iC3b complex in Mn^{2+}, with a very similar elution profile as compared to that obtained in Mg^{2+}. **D.** SPR sensorgrams for the interaction of CR3 injected on an iC3b surface using a Mg^{2+} buffer. CR3 was injected at 100, 50, 25, 12.5, 10, 5, 2.5, 1.25, 0.625, 0.3125 nM. The raw curves are shown in grey and the fit is shown in red. The dissociation constant calculated as $K_D=k_{off}/k_{on}$ is indicated. The on- and off-rates are the average of three independent experiments. **E.** As in panel D, but in a Mn^{2+} buffer, only curves for CR3 concentrations 25, 12.5, 10, 5, 2.5, 1.25, 0.625. 0.3125 nM are shown.

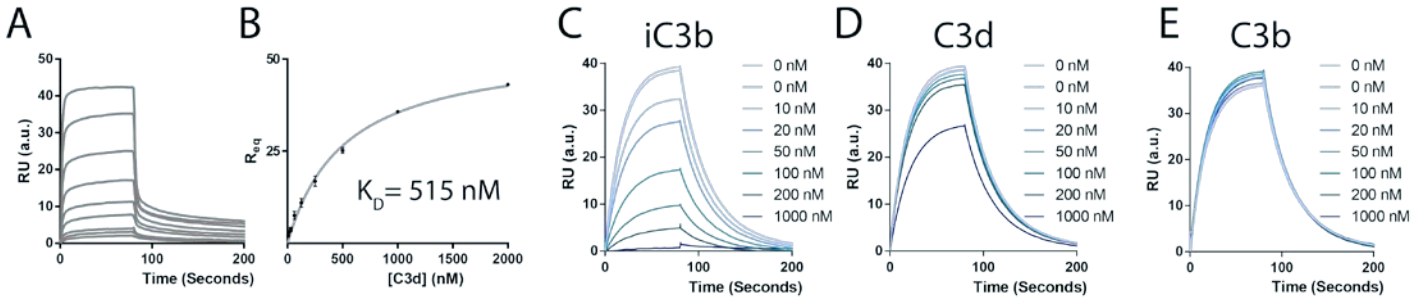

Figure 4. Analysis of the interaction between C3d and CR3. A. Sensorgrams from an SPR experiment where CR3 at 2000, 1000, 500, 250, 125, 62.5, 31.25, 15.63, 7.81 nM was injected on a C3d surface. **B.** Steady-state analysis of SPR experiments as displayed in panel A. Average values ± the standard deviation for three repetitions are plotted, and the K_D value is determined by non-linear regression. The resulting K_D value is more than 15 fold higher than the K_D determined for the CR3:iC3b complex. **C-E.** Sensorgrams of SPR competition assays where 20 nM of CR3 was pre-incubated with variable concentrations of iC3b (**C**), C3d (**D**), or C3b (**E**) before being injected unto an iC3b surface.

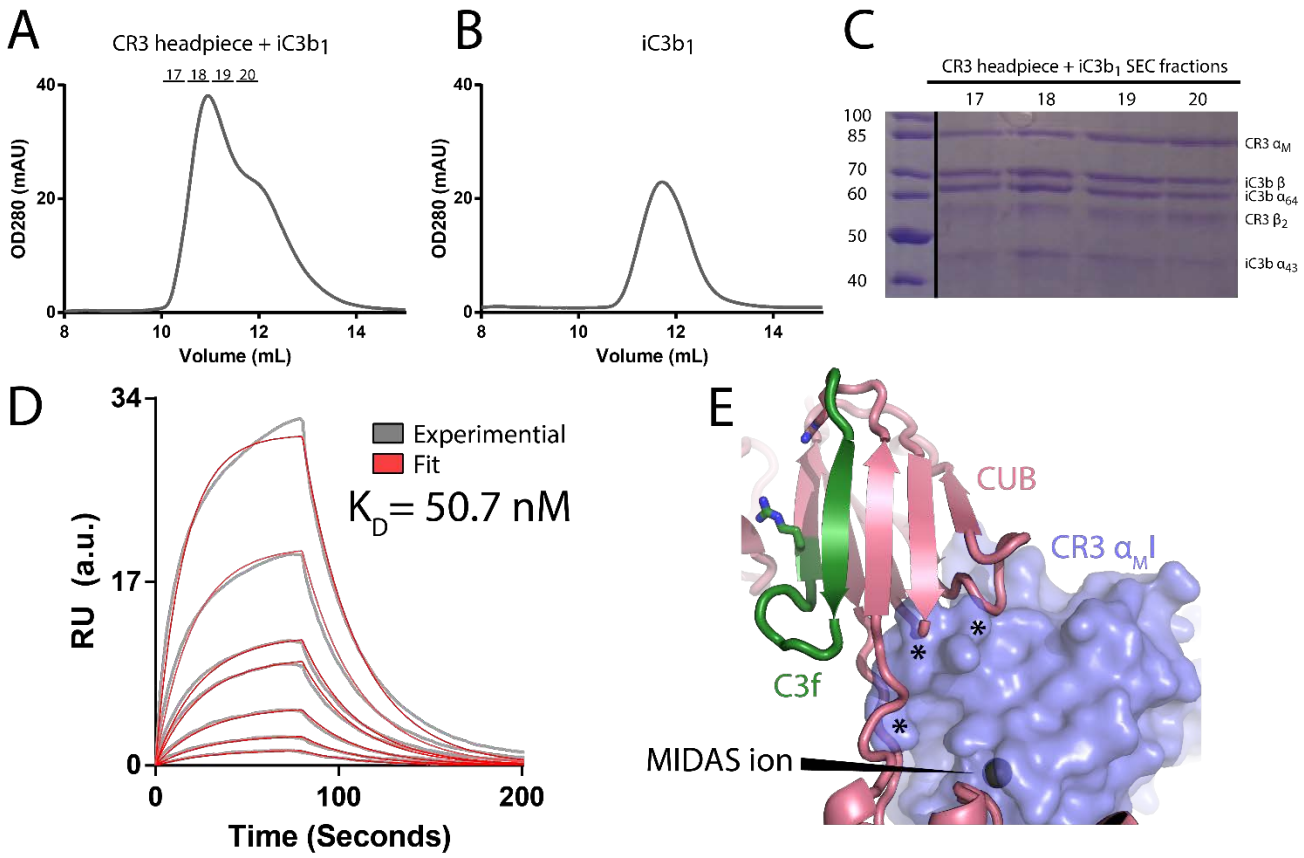

Figure 5. Characterization of the CR3:iC3b$_1$ complex. A. SEC analysis of complex formation between CR3 and iC3b$_1$. **B.** Control SEC chromatogram for iC3b$_1$ only. **C.** SDS-PAGE analysis of fractions from panel A verifying that a complex is formed between iC3b$_1$ and CR3. **D.** SPR analysis of CR3 injected on an iC3b$_1$ surface. CR3 was injected at 50, 25, 12.5, 10, 5, 2.5, 1.25 nM. The K_D value determined is comparable to the K_D determined for the iC3b:CR3 complex. The dissociation constant is calculated as $K_D=k_{off}/k_{on}$. The on- and off-rates are the average of three independent experiments. **E.** A significant overlap (marked with *) will occur between the iC3b$_1$ CUB domain and the CR3 α_MI domain if the CUB domain adopts a C3b like structure. Hence, the iC3b$_1$ CUB domain is likely to relocate or rearrange upon CR3 binding. The C3f fragment released after the second cleavage is displayed in green.

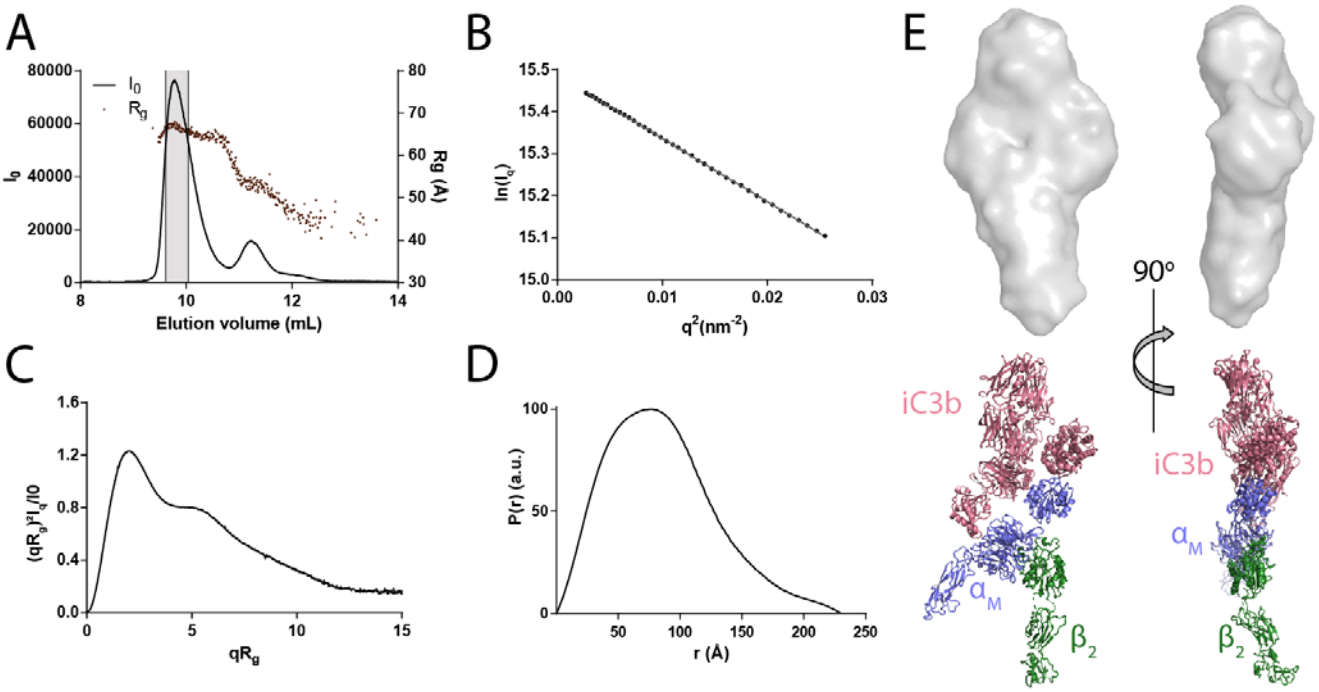

Figure 6. SEC-SAXS analysis of CR3 in complex with either iC3b. A. The forward scattering and R_g of each frame during the SEC-SAXS experiment of the CR3:iC3b complex plotted as a function of the elution volume. Two peaks are identified corresponding to the CR3:iC3b complex and free iC3b. The scattering curve for the CR3:iC3b complex was generated from the shaded area. **B.** Guiner plot of the scattering curve for the CR3:iC3b complex. **C.** The Guinier normalized Kratky plots for the CR3:iC3b complex indicates that the complex has limited flexibility. **D.** The pair distribution function of the CR3:iC3b complex suggesting a D_{max} of 225 Å for the CR3:iC3b complex. **E.** Average model of 10 ab initio models calculated from the CR3:iC3b SEC-SAXS data. A putative CR3:iC3b complex prepared by hand independent of the SAXS data is shown below to scale, illustrating the possible dimensions of a CR3:iC3b complex.